Eur. Phys. J. D **11**, 309–320 (2000)

THE EUROPEAN
PHYSICAL JOURNAL D
EDP Sciences

Study of a X-ray laser-plasma source for radiobiological experiments: microdosimetry analysis and plasma characterisation

F. Bortolotto[1,2], D. Batani[1,a], F. Previdi[3], L. Rebonato[3], E. Turcu[4], and R. Allott[4]

[1] Dipartimento di Fisica “G. Occhialini”, Università degli Studi di Milano, Bicocca and INFM UdR Milano Bicocca, Via Emanueli 15, 20126 Milano, Italy
[2] Max-Born-Institut für Nichtlineareoptik und Kurzzeitspektroscopie, Max-Bornstr. 2a, 12489 Berlin-Adlershof, Germany
[3] Dipartimento di Elettronica e Informazione, Politecnico di Milano, and INFM UdR Milano Bicocca, 20126 Milano, Italy
[4] Rutherford Appleton Laboratory, Chilton Didcot, Oxon, OX11 OQX, UK

Received 16 September 1999 and Received in final form 1st February 2000

Abstract. A soft X-ray laser-plasma source, used in radiobiology experiments with yeast cells, was characterised with flat crystal spectrometers and P-I-N diodes, obtaining an absolute measurement of the emission spectrum. A comparison with the results of simulations performed with the code RATION allowed the characterisation of the emitting plasma. A model for the energy deposition in yeast cells was developed to take into account the different cell structures (wall-membrane complex, cytoplasm and nucleus). Dose calculations performed considering the source emission spectrum were compared with direct measurements of transmission through plastic foils and allowed to verify the hypothesis of preferential dose deposition in the outer cellular regions.

PACS. 87.50.-a Effects of radiation and external fields on biomolecules, cells and higher organisms – 42.55.-f Lasers – 52.25.Nr Emission, absorption, and scattering of X and γ radiation

1 Introduction

In recent years, X-ray emission from laser produced plasmas has been much studied. This kind of research has three main motivations:

(i) plasma physics, X-ray emission being used to characterise plasma parameters (electronic density and temperature, ionisation degree);
(ii) atomic physics, the study of X-ray line emission giving information on the energy levels in multicharged ions;
(iii) applications of laser-plasmas as soft X-ray sources.

In particular laser-plasma sources have been used to study the radiation induced damage in biological materials, a classical domain of biophysical research [1]. In this context, an experiment was recently performed at Rutherford Appleton Laboratory to irradiate yeast cells with soft X-rays produced by laser irradiation of Teflon targets [2–4]. The low penetration depth of the soft X-rays used in the experiment allowed a preferential energy deposition in the cell wall and cytoplasm as compared to the nucleus, with the goal of minimising the interference with DNA activity. Since the cytoplasm plays an important role in the anaerobic metabolic processes (fermentation) of yeast cells [5,6], an on-line monitoring of CO_2 production by a population of yeast cells was adopted as an easy and efficient technique to investigate the effects of irradiation [4]. To analyse the dose deposition inside the different cell compartments, it is necessary to perform a complete characterisation of the X-ray spectrum and develop a realistic cellular model that takes into account the specific structures of yeast cells [6–8].

In this work we present a detailed study of the emission spectrum of the laser plasma X-rays source and develop a model for the dose deposition in yeast. A theoretical modelisation of the spectrum is important not only to characterise the source, but also to estimate those components of X-ray emission which were not directly detectable. In our experiment this problem arises in particular with respect to low energy emission and also in connection to the presence of hard X-rays which are expected as a consequence of the high laser intensity [9, 10].

The cellular model, based on the characterisation of yeast cells performed in [8], allowed the calculation of the doses to the cell wall, cytoplasm and nucleus separately, so that it is possible to evaluate the damage induced to the different cellular compartments.

---

[a] e-mail: `batani@mi.infn.it`

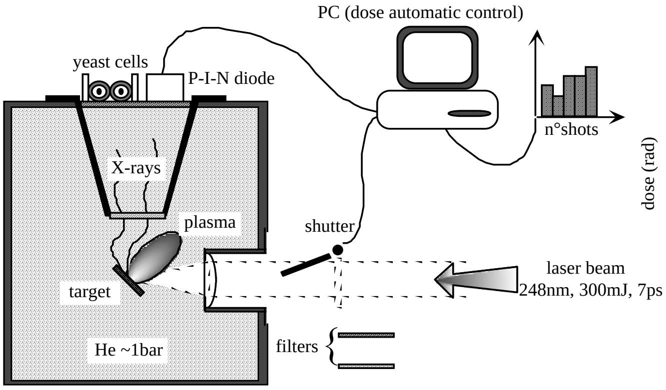

Fig. 1. Experimental set-up.

2 Experimental set-up

The experimental set up is described in [1]. The laser system produces a pulse train of 16 pulses, each 7 ps long and spaced by 2 ns intervals, with a 20 Hz repetition frequency and a wavelength of 0.248 μm. The pulse train energy is of the order of 300 mJ giving an intensity on target of about 5×10^{15} W cm^{-2} on a focal spot of about 30/50 μm diameter. The focal spot size was determined from images obtained with a pin-hole camera used to image the generated hot plasma. The irradiation set-up is shown in Figure 1: the laser is focused onto the target (a tape driven by a DC electric motor) to produce a hot and dense plasma, whose emission falls in the X-UV range. This irradiates the biological samples and is also recorded by a P-I-N diode, placed after the same filters interposed between the source and the cells, to measure the delivered dose. The dose of subsequent shots is summed by a computer control that triggers a shutter in order to stop the irradiation once the desired dose value is obtained. The P-I-N diode had a time resolution of about 1 ns which, coupled to a fast oscilloscope, allowed the observation of the single X-ray pulses generated by each ps pulse of train (however the single pulses could not be time-resolved).

For the purpose of the experiment we needed a radiation that could be mainly stopped inside the cellular wall and the cytoplasm: the undesired radiation is then characterised by a high penetration depth in biological matter and falls in the water-window region (the energy range within the carbon absorption edge at 280 eV and the oxygen absorption edge at 532 eV) and in the high energy range (> 1 keV).

We choose a Teflon (CF_2) target because the fluorine emission spectrum is centred at 0.9 keV. Moreover it also presents the additional advantage that in this spectral range it has a K-shell emission (which, with its few lines, simplifies the dose calculations) and that it can be produced in thin stripes (100 μm thick). Unfortunately, it has the problem of carbon emission in the water-window region. To cut-off such undesired X-ray emission an appropriate filtering is needed, which was obtained by means of plastic filters with thickness of a few microns with a thin metallic deposition.

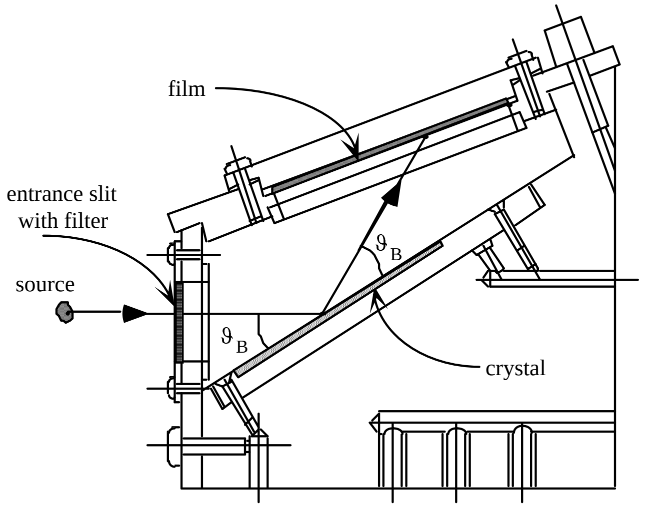

Fig. 2. Flat crystal Bragg mini-spectrometer (approximately real size).

During the experiment we used two different set of filters:

- an "aluminium" one, composed by a first hostaphan filter (1 μm) and a mylar filter (1 μm) covered on both sides by a 0.1 μm Al deposition;
- a "copper" one, composed by a parylene filter (2 μm) with a Cu deposition of 0.3 μm on each side.

As it will be shown later, the Al filter greatly reduces the undesired radiation in the energy range below 532 eV (O absorption edge) while the Cu filter, due to the CuL-absorption edge at 933 eV [11], grants a reduction even in the higher energy range, thus allowing irradiation by photons in a narrower energy range.

Finally, in order to minimise damages caused by debris emission from the target [12] a helium flow, at about 1 bar pressure, is blown from the lens holder onto the target surface. It also contributes to radiation filtering.

3 X-ray spectrometry

A flat crystal spectrometer (represented in Fig. 2) was used to disperse the X-ray radiation and the spectrum (Fig. 3) was recorded on a Kodak DEF film. The obtained spectra are space and time integrated so any X-ray emission produced during the duration of the laser pulse train is recorded. To prevent film exposition by visible light, an opaque filter is placed onto the spectrometer entrance slit (1 μm hostaphan + 1 μm parylene + 3 μm Al).

For a correct interpretation of the spectrum it is necessary to identify the different lines on the film. To facilitate line recognition, the filter had a Cu layer (5 μm) on half slit, giving a wavelength fiducial at 0.933 keV (CuL-absorption edge).

Moreover the absolute spectrum has to be obtained from film densitometry with a deconvolution that takes into account filter and gas buffer transmission, crystal reflectivity and film sensitivity. These quantities are all

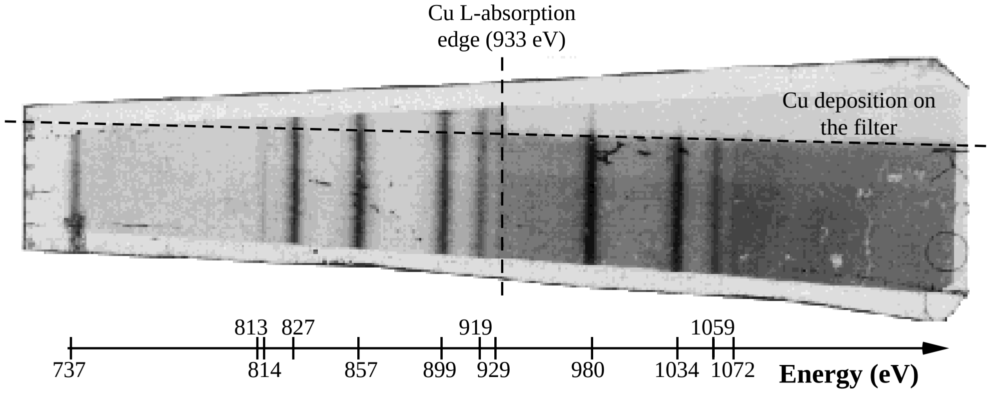

Fig. 3. X-ray spectrum emitted from Teflon target and recorded on Kodak DEF film. Typically about 350 laser shots were needed to obtain a good spectrum.

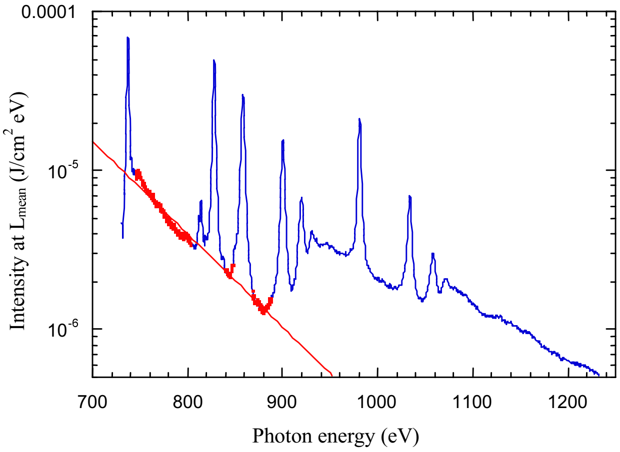

Fig. 4. Deconvoluted spectrum: the fluorine H-like and He-like groups of lines are indicated and the recombination exponential part at low temperature is evidenced. The fit to this part gives $0.16503\exp(-h\nu/74.27)$. At high temperature the bremsstrahlung tail gives a fit $0.00764\exp(-h\nu/128.17)$.

Table 1. Comparison between experimental values of lines wavelength and those tabulated [20].

λ_{experim}	$\lambda_{\text{tabulated}}$	$\Delta\lambda/\lambda$ (%)	Ion	Configuration
16.814	16.807	0.04	$\mathrm{F}^{\mathrm{VIII}}$	$1s2p \rightarrow 1s^2$
15.231	15.246	0.10	F^{VIII}	$2p^2 \rightarrow 1s2p$
	15.224	0.04	F^{VIII}	$2s3p \rightarrow 1s2s$
14.973	14.982	0.06	F^{IX}	$2p4p \rightarrow 1s4p$
14.448	14.458	0.07	$\mathrm{F}^{\mathrm{VIII}}$	$1s3p \rightarrow 1s^2$
13.771	13.781	0.07	$\mathrm{F}^{\mathrm{VIII}}$	$1s4p \rightarrow 1s^2$
13.480	13.488	0.06	$\mathrm{F}^{\mathrm{VIII}}$	$1s5p \rightarrow 1s^2$
13.318	13.334	0.12	$\mathrm{F}^{\mathrm{VIII}}$	$1s6p \rightarrow 1s^2$
12.636	12.643	0.20	F^{IX}	$3p \rightarrow 1s$
11.995	11.989	0.05	F^{IX}	$4p \rightarrow 1s$
11.720	11.707	0.11	F^{IX}	$5p \rightarrow 1s$
11.563	11.560	0.02	F^{IX}	$6p \rightarrow 1s$

wavelength dependent and the film response is also a function of the radiation intensity. The models used in the deconvolution referring to our specific experimental conditions are described in the Appendix A.

The filter and gas buffer transmission coefficient, as well as the absorption coefficients used in calculating film response, have been obtained by means of the code RATP [13], which uses Henke's data for absorption coefficients [14]. This code calculates transmission coefficients as a function of radiation wavelength once the chemical formula, the density and the thickness of the considered material are known.

4 Spectrum analysis

4.1 Deduction of electronic temperature from experimental spectrum

Figure 4 shows the deconvoluted spectrum in which we marked the Fluorine H-like and He-like groups of lines (K-shell spectrum). In Table 1 we show the comparisons between the experimental values of lines wavelength and those tabulated in [15].

The carbon K-shell spectrum was not recorded, since its lines are below the range observable with a RbAP crystal. However, the presence of C-ions in the plasma necessarily implies both carbon line emission and electron recombination on carbon levels. Such a recombination will appear in our experimental spectrum as an exponential trend, superimposed to the F-ions lines; moreover, recombination on F-energy levels and bremsstrahlung emission will appear as an exponential tail at higher energies. We will see in Section 4.3 that the computer simulations of our spectrum confirm this hypothesis.

The exponential interpolation of the continuum regions of the spectrum at low energies (see Fig. 4) gives a value of electronic temperature $T_{\mathrm{e}} = (74 \pm 0.05)$ eV. Subtracting such a recombination emission we obtain a "pure" fluorine spectrum whose bremsstrahlung tail implies an electronic temperature $T_{\mathrm{e}} = (130.8 \pm 1.2)$ eV. The effect of removing the continuum at low energies does not affect this value very much, since the lower energy recombination emission decreases with photon energy following an exponential law; indeed, if we do not remove it, we would get $T_\mathrm{e} \approx 128$ eV.

We interpret the difference between the two electronic temperatures of the plasma emitting in the different spectral ranges as a spatial effect: the harder emission arising essentially from the plasma region with higher temperature. This is consistent with the usual picture of laser-plasma interaction which describes a plasma with a complex temperature (and density) profile arising both from plasma expansion and laser intensity profile.

We also note that at the higher temperature corresponding to F-emission, carbon is completely ionised and cannot appreciably contribute to X-ray emission. Hence carbon emission must originate from the colder plasma layers.

4.2 Deduction of electronic density from experimental spectrum

Once an absolute calibration of the recorded spectrum is obtained, it is also possible to deduce the value of electronic density n_e from the bremsstrahlung tail, which corresponds to the part of the spectrum at photon energies higher than the maximum ionisation value $RhcZ_\mathrm{F}^2 = 1103.09$ eV. Indeed the intercept of such curve on a semi-logarithmic graph is related to n_e. More precisely the source emission per unit volume and unit photon energy (in $\mathrm{W\,cm^{-3}\,eV^{-1}}$) for free-free transitions is given as [16,17]:

$$\frac{\mathrm{d}\varepsilon_{ff}}{\mathrm{d}h\nu} = 1.5 \times 10^{-32} \frac{n_\mathrm{e}}{T_\mathrm{e}^{1/2}} \exp(h\nu/T_\mathrm{e}) \sum_i N_i Z_i^2 \quad (1)$$

where N_i and Z_i are respectively the ionic density and the ion charge, the sum being extended over all the ionic species in the plasma.

The recombination emission (free-bound transitions) has to be added. This is given by [17]:

$$\frac{\mathrm{d}\varepsilon_{ff}}{\mathrm{d}h\nu} = 1.5 \times 10^{-32} \frac{n_\mathrm{e}}{T_\mathrm{e}^{3/2}} \sum_i N_i Z_i^2 \sum_{n=1}^{\infty} \frac{J_i^{(n)}}{n^3} I_i^{(n)} \times \exp\left(-\left(h\nu - I_i^{(n)}\right)/T_\mathrm{e}\right) \chi\left(h\nu - I_i^{(n)}\right) \quad (2)$$

where n is the principal quantum number of the level to which the recombination occurs, $J_i^{(n)}$ is the number of vacancies in the quantum state n before recombination, $I_i^{(n)}$ is the ionisation energy of the ion from the quantum state n and Z_i is the ion charge before recombination. The summation over n accounts for recombination into different possible quantum states of the ion i. The step function $\chi(h\nu - I_i^{(n)})$ is zero for $h\nu \leq I_i^{(n)}$ and unity for $h\nu \geq I_i^{(n)}$.

Considering the limit for $h\nu \geq \max\{I_i^{(n)}\}$ (for which $\chi(h\nu - I_i^{(n)}) = 1$ for all i and n) of the sum of free-free and free-bound transitions, and formally evaluating it at $h\nu = 0$ (*i.e.* considering the intercept value), we obtain

$$\frac{\mathrm{d}\varepsilon_{ff}}{\mathrm{d}h\nu} = 1.5 \times 10^{-32} \frac{n_\mathrm{e}}{T_\mathrm{e}^{3/2}} \times \left[\sum_i N_i Z_i^2 \left(T_\mathrm{e} + \sum_{n=1}^{\infty} \frac{J_i^{(n)}}{n^3} I_i^{(n)} \exp\left(+I_i^{(n)}/T_\mathrm{e}\right)\right)\right]. \quad (3)$$

Since an absolute calibration is needed, it is necessary to introduce a scale factor K, depending on our specific experimental parameters, which divides the calculated plasma emission. In facts, the deconvoluted experimental spectrum gives the emission spectral intensity per unit photon energy (in $\mathrm{J\,cm^{-2}\,eV^{-1}}$) at the mean distance between the source and the film ($L_\mathrm{mean} = 8.9$ cm). Thus $K = 2\pi L_\mathrm{mean}^2 / V_\mathrm{p} t_\mathrm{X}$ where V_p is the volume of the emitting plasma (half sphere) and t_X is the total duration of X-ray emission. Hence considering a plasma dimension close to the laser focal spot diameter (≈ 35 μm), the number of laser shots typically used to record a well contrasted spectrum ($\approx$ 300–400) and a single X-ray pulse duration ($t_\mathrm{X} = 50$ ps as measured in [1] for our source) we obtain $K = 2.53 \times 10^{18}\ \mathrm{cm^{-1}\,s^{-1}}$.

Finally, some approximations are needed to evaluate the sums over the ionic populations and over atomic levels at the different ionisation degrees.

The mean ionisation degree could be estimated following [18] as $\widetilde{Z}^* = (2/3)(\widetilde{A}T_\mathrm{e})^{1/3} = 8.65$, where $\widetilde{A} = (2/3)A_\mathrm{F} + (1/3)A_\mathrm{C}$ is the mean atomic weight of Teflon (66% F and 33% C). We note that the obtained value is greater than the maximum ionisation degree of the plasma *i.e.* $(2/3)Z_\mathrm{F} + (1/3)Z_\mathrm{C} = 8$; hence we considered the Teflon plasma as constituted of fully ionised atoms and in the following used $\widetilde{Z}^* = 8$ as the mean ionisation degree.

To evaluate the sums over n we remind that, for fully ionised atoms $J_i^{(n)} = 2n^2$ (degeneracy of the nth level) and $I_i^{(n)} = RhcZ^2/n^2$ so the argument of the sums over n, for both the species F and C, is

$$\frac{2Rhc}{n^3} \exp\left(\frac{RhcZ^2}{T_\mathrm{e} n^2}\right)$$

which implies that the terms with $n > 1$ are negligible. With these assumptions the quantity in square brackets in equation (3) (the sums over i and n) simply becomes

$$N_i^\mathrm{F} Z_\mathrm{F}^2 RhcZ_\mathrm{F}^2 \exp(RhcZ_\mathrm{F}^2/T_\mathrm{e}) + N_i^\mathrm{C} Z_\mathrm{C}^2 RhcZ_\mathrm{C}^2 \exp(RhcZ_\mathrm{C}^2/T_\mathrm{e}). \quad (4)$$

Nothing that $n_\mathrm{e} = N_i^\mathrm{tot} \widetilde{Z}^*$ (where $N_i^\mathrm{F} = (2/3)N_i^\mathrm{tot}$, $N_i^\mathrm{C} = (1/3)N_i^\mathrm{tot}$), and substituting the numerical values, this term can be expressed as a function of electronic density giving a value $= 8.15 \times 10^7 n_\mathrm{e}$. By inserting this in equation (3) and equating it to the experimental intercept ($7.64K \times 10^{-3}$), we obtain a value of electronic density $n_\mathrm{e} = 4.2 \times 10^{21}\ \mathrm{cm^{-3}}$.

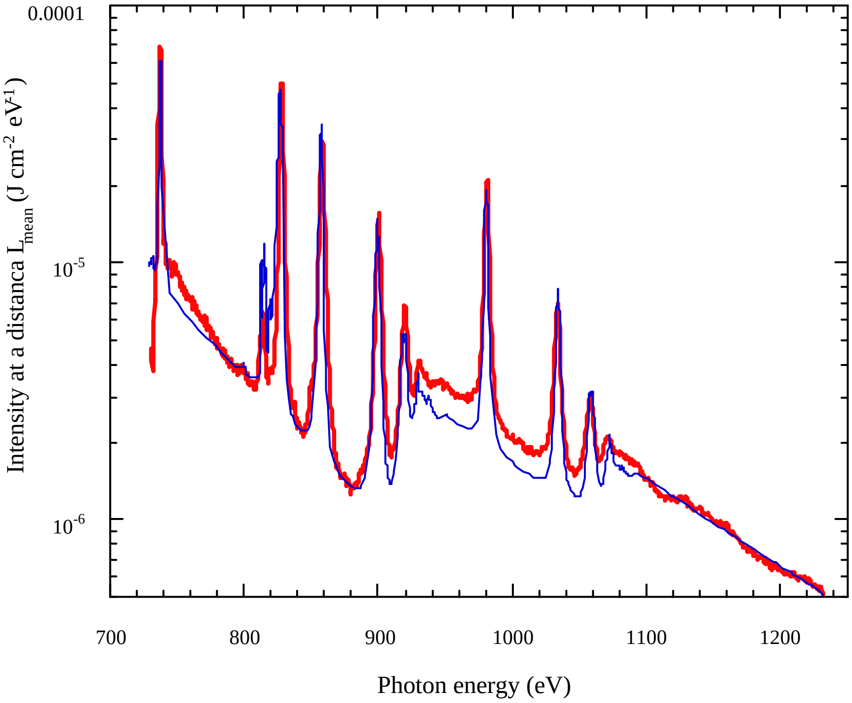

Fig. 5. Comparison between experimental and simulated spectra.

4.3 Spectrum simulation with the RATION code

To get a better confidence in the plasma parameters calculated from the experimental spectrum and also to have an estimation of the non-recordable emission at low energy, we simulated Teflon plasma emission by means of the code RATION [19]. This code, developed at Lawrence Livermore National Laboratory, allows the study of K-shell spectroscopy (ionisation stages from Li-like to H-like) of atomic species from carbon ($Z = 6$) to iron ($Z = 26$).

The experimentally estimated values of plasma parameters that we used for the simulation are: $T_e = 130$ eV, $n_e = 4 \times 10^{21}$ cm^{-3}, a plasma composition at 66% F and 33% C, a plasma dimension near focal spot diameter ≈ 35 μm and a mean instrumental FWHM (the projection of crystal rocking angle on the film plane) of about 1.2 eV.

The agreement is quite good: not only the continuum and the tail are well reproduced, but also the line ratios are respected. As for the absolute values of continuum emission the maximum discrepancy is 20%.

Figure 5 shows the comparison between the experimental and the simulated spectra where the recombination continuum at low energies has been added. From the comparison between the two continua, we can deduce the parameters of the plasma emitting in the low energy range. We recall that, in a simplified picture, our plasma can be considered as spatially divided in two different regions at different temperatures.

In the conditions of low energy emission ($T_e = 74$ eV) the mean ionisation degree of fluorine atoms is $Z_F^* = 7.7$. Assuming that the fluorine ions present in the plasma have a ionisation degrees 7 (ground state recombination edge at 185.185 eV [20] and 8 (ground state recombination edge at 953.84 eV [20], we obtain that 26% of the total fluorine ionic population has a ionisation degree 7. Due to their high recombination energy, F atoms with ionisation degree 8 contribute to the emission only in the higher energy range where the low temperature spectrum is not experimentally distinguishable from the high temperature one. Hence in the low energy range ($\approx$ 700–800 eV) the only appreciable contributions are those due to the recombination on the ground states of fully ionised C atoms and 7 times ionised F atoms.

On the basis of such hypotheses, following what we did in the previous section, the last term in equation (2) becomes $1.81 \times 10^6 n_e$. In the case of emission of high energy, we assumed a plasma size of the order of the low focal spot, in line with the qualitative idea that the region of the plasma directly heated by the laser is the hottest one. This allowed the electron density n_e to be obtained. In the case of emission at low energy, we considered a lower temperature plasma with unknown size and, fixing typical values for our experimental conditions, we obtained the results of Table 2.

Finally using the values in Table 2 as input parameter for the RATION, we could calculate the "expected" low energy emission produced from C ions in the spectral region ($h\nu < 700$ eV) which could not be directly detected experimentally. As shown in Figure 6 this is a K-shell spectrum produced from H-like and He-like C ions. Lines are broader than for F-like spectrum due to the higher plasma density (Tab. 2). We could hence calculate the energy emitted in the water window region and verify, as expected (see Tab. 2 again), that the larger percentage of plasma emission lies at very low energy (and is also almost

Table 2. Values of plasma dimension and related electronic density for the colder plasma layer. These data has been used to obtain three different C spectra by means of RATION code. The third and fourth columns show the relative ratios of the energy flux in the low energy region (below 700 eV) and in the whole spectrum. The whole spectrum is obtained by adding the low energy region to the experimental spectrum.

∅ plasma (μm)	n_e (cm^{-3})	(%) Intensity in the low energy region	Transmission (%) Cu filter	Transmission (%) Al filter
52	4.2×10^{21}	95	0.17	1.3
35	7.6×10^{21}	97	0.16	1.2
20	1.8×10^{22}	98	0.15	1.1

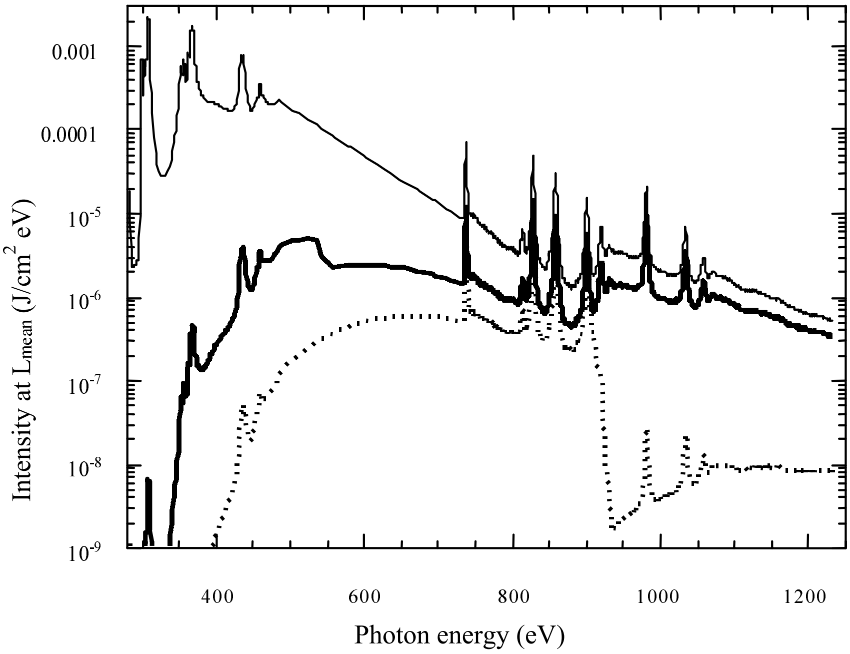

Fig. 6. Effect of filtering with the Al and Cu filter on the reconstructed spectrum: carbon emission (200 to 700 eV) was obtained by means of the RATION code and added to the experimental spectrum (700 to 1200 eV). The grey and dotted curves correspond to Al and Cu filtering respectively.

independent on the specific parameters of low temperature plasma which are considered). Values of electron density up to the laser critical density (1.8×10^{22}) have been considered since this is the maximum value at which laser interaction can take place and typically has been seen to play a role in X-ray emission from laser plasmas.

Figure 6 and Table 2 also show the effect of the two different sets of filters used during the experiment on the simulated spectrum. It is possible to see that both filtering are efficient in cutting-off the undesired emission in the water window region and, in particular, the Cu filter greatly reduces the > 0.9 keV photons flux too.

4.4 Hard X-ray emission

As a consequence of the high intensity laser irradiation and of resonant absorption, a suprathermal electronic population is produced as shown in many theoretical and experimental works [21, 22]. This changes the electronic velocity distribution in the plasma, originating a larger number of high energy electrons with respect to those expected from a Maxwell distribution. These produce high energy photons changing the spectral distribution of bremsstrahlung radiation. In most cases, the velocity distribution of such suprathermal electrons can be considered to be a Maxwellian with a typical temperature T_h (in eV) given by:

$$T_h = 0.215(I_L\lambda_L^2)^{1/3} \tag{5}$$

where I_L and λ_L are the laser intensity (in W cm^{-2}) and wavelength (in μm) respectively. This scaling law was established more than 15 years ago [22,23] and was recently verified to hold even at intensities as high as 10^{19} W/cm^2 in the work by Beg *et al.* [9].

The spectrum of the radiation emitted from such suprathermal electrons is still described by equation (1) with a temperature T_h (in our case $T_h \approx 14$ keV). Thus the suprathermal emission is

$$\frac{\mathrm{d}\varepsilon_{\mathrm{h}}}{\mathrm{d}(h\nu)} = 1.5\times10^{-32}\frac{n_{\mathrm{h}}}{T_{\mathrm{h}}^{1/2}}\sum_i N_i Z_i^2 \exp(-h\nu/T_{\mathrm{h}})$$

$$\approx 1.5\times10^{-32} n_{\mathrm{h}} \frac{N_i^{\mathrm{tot}}(\widetilde{Z}^*)^2}{T_{\mathrm{h}}^{1/2}}\exp(-h\nu/T_{\mathrm{h}}). \quad (6)$$

Since the suprathermal tail is due to the bremsstrahlung of the suprathermal electrons, all ions in the plasma contribute in decelerating them, and then simply $\sum_i N_i Z_i^2 = n_{\mathrm{e}}\widetilde{Z}^*$. The suprathermal electron density is a fraction of the total electron density which can be estimated by looking at previous works [9,10] as between 0.01 and 0.1 times the electronic density of the plasma. Substituting the values $n_{\mathrm{e}} = 4.2\times10^{21}$ cm^{-3}, $\widetilde{Z}^* = 8$, $n_{\mathrm{h}} = 0.1 n_{\mathrm{e}}$ and $T_{\mathrm{h}} = 1.4\times10^4$ eV, we note that, even in case the largest number of suprathermal electrons is consider, the contribution of suprathermal electrons is more than two orders of magnitude lower than that due to the Maxwellian electrons. This is the reason why in the recorded spectrum, at energy from 700 to 1200 eV, the suprathermal tail is not observable. However such contribution becomes predominant at high energies.

To assess the amount of suprathermal electrons in our plasma more precisely, it is necessary to refer to the experimental measurements of radiation attenuation through different thickness of parylene, presented in the next section.

5 Energy deposition in organic material

In order to cross-check our absolute calibration of the emission spectrum, we performed direct measurement of radiation attenuation through different thickness of plastic material. This analysis is also essential in order to understand the absorption of plasma radiation in organic matter similar to the biologic material of yeast cells. Finally the comparison of the results obtained from our "reconstructed" spectrum with experimental data allows us to estimate the amount of suprathermal electrons in the plasma.

The experimental set-up is the same described in Section 2 but, instead of biological samples, plastic layers (parylene $[\mathrm{C_8H_8}]n$, $\rho = 1$ g cm^{-3}) of different thickness have been used and a second P-I-N diode, reading the attenuated radiation on the back of plastic, has been added. The total charge collected from the two P-I-N diodes, with and without a thickness x of material, is thus equal to the ratio between the radiation intensities:

$$\frac{I(x)}{I_0} = \frac{Q_2}{Q_1}\,. \quad (7)$$

Between the source and the P-I-N diodes (at a distance $L = 31.7$ cm) there are the gas buffer and the Cu filter already described in Section 2 and considered for absolute calculations.

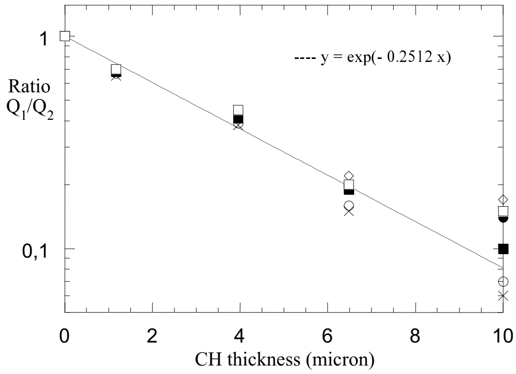

Fig. 7. Comparison between experimental data and those calculated corresponding to different suprathermal electron populations. (□) Experimental data, (×, ○, ■, ●, ◊) numerical results corresponding to $n_{\mathrm{h}} = 0$, 1, 10, 15, 20% respectively. The continuous line is the interpolation of experimental data for plastic thickness ≤ 6 μm.

We remind that the P-I-N sensitivity (in C/J) is given by:

$$S = (e/\Delta\varepsilon)\exp(-\mu d)\left[1-\exp(-\mu D)\right] \quad (8)$$

where $\Delta\varepsilon = 3.62$ eV is the energy for the creation of an electron-hole pair in Si, e is the electronic charge, μ is the Si absorption coefficient, and finally d and D are, respectively, the thickness of the dead layer and of the active region of the P-I-N diode.

Hence the charge collected by the diode is:

$$Q = \int AS(h\nu)I(h\nu)T(h\nu)d(h\nu)\mathrm{d}\nu \quad (9)$$

where I (in J cm^{-2} eV^{-1}) is the radiation intensity per unit photon energy falling on the diode, A (in cm^2) is the diode surface and T is the overall transmission coefficient of the interposed absorbers. In the experiment two 100 P-I-N–125 P-I-N diodes have been used, with typical parameters: $d = 0.75$ μm, $D = 125$ μm and $A = 1$ cm^2. The transmission coefficients of filter, gas buffer and plastic, as the Si absorption coefficients, have been obtained with the RATP code.

Figure 7 shows the experimental results obtained for the ratio Q_1/Q_2 and the ratios calculated from reconstructed spectra which include the emission of suprathermal electrons. The errors on the experimental points can be calculated through the standard derivation of the experimental data (on y-axis) and the thickness of the plastic foils used as absorbers (on x-axis). As an estimation of the errors in abscissa we have considered the confidence of ±5% given by the producer [29] for their thin plastic foils. Let's note that the standard deviation on the experimental points could be underestimated since it was calculated on a few data.

As shown in Figure 7, the value $n_{\mathrm{h}} = 0.15 n_{\mathrm{e}}$ for the suprathermal tail is the one that fits the experimental data better. This is not very far from values already reported in literature [9, 10]. We will consider this result in the dosimetric calculations of the next section. Anyway we see that the suprathermal electron emission does not affect very much the dose delivered to yeast cells, corresponding to photon energies that have a penetration in biological material higher than the mean cell dimension. Also, if we make an exponential interpolation of the first four experimental data of Figure 7, we can conclude that the radiation behaves through the parylene essentially as a monochromatic beam with photon energy ≈ 900 eV, until a thickness of 6.5 μm is reached. Indeed the parylene absorption coefficient evaluated from this interpolation (*i.e.* the slope of the exponential law on a logarithmic scale) is $\mu = 2512$ cm^{-1}, corresponding to photon energy $h\nu = 938$ eV. In other words the energy deposition in biological material as a function of thickness is the same which would be obtained from a X-ray monochromatic beam with this photon energy. This behaviour is mainly due to the Cu-filter that cuts-off the hard components of the spectrum.

6 Dosimetry on yeast cells

Once the source spectrum is known, it is possible to calculate the doses delivered to the different cells compartments.

The integral doses absorbed by the nucleus, the cytoplasm and the wall-membrane complex, as well as by an "average" undifferentiated cell, have been calculated using an experimental attenuation of radiation in matter (Lambert-Bouguet-Beer law) [25] and the absorption coefficients obtained with the RATP code [13].

Cellular parameters are described in [8], the wall-membrane complex, constituted by tightly packed protein, has been considered as composed of pure biological matter (with "molecular formula" $C_{92}H_{149}O_{30}N_{25}S$).

Considering a spherical cell divided in three compartments is a clear progress with respect to the approach normally used in radiobiology (see for instance [26]) where only the radiation penetration depth in the undifferentiated biological material and the average dose to the whole cell (or equivalently the surface dose) are calculated. In our case instead we have some hints on where the dose is actually deposited and what damages it is likely to produce.

The dose calculation cannot be performed analytically because it requires the integration of exponential functions with different exponents in the various cell compartments and also because the symmetry of the cell is spherical while the radiation beam is cylindrical. Hence, we have written a computer program which is described in Appendix B together with the evaluation of the doses.

As expected, the ratio between the dose delivered to the inner cell structures and the dose to the wall-membrane complex increases with photon energies, due to higher penetration. For instance, Table 3 shows the comparison between monochromatic radiation at 0.9 keV (mean photon energy from the Teflon target) and at 1.5 keV. This last corresponds to the mean photon energy which would be obtained with an Al target.

Table 3. Ratios of the doses delivered to nucleus and cytoplasm respect of wall-membrane complex for two monochromatic radiation, 0.9 keV and 1.5 keV.

Dose ratio	$E = 0.9$ keV	$E = 1.2$ keV
nucleus/wall	0.593	1.188
cytoplasm/wall	0.966	1.370

With Teflon targets, the radiation is mostly absorbed in the outer compartments, however there is still a non negligible absorption in the cell nucleus. The real situation is even worse because the Teflon spectrum has several lines superposed to a continuum at high energy and these photons are characterised by different absorption coefficients. Hence the less energetic ones are mainly absorbed in the cell wall-membrane complex, while the harder photons are characterised by a lower absorption coefficient and thus by a larger penetration in biological matter. Hence they can travel through the cell with much lower attenuation and are more likely to deposit their energy in the cell nucleus (the X-ray spectrum becomes harder as it goes through the biological material) [5,27]. This problem was solved by using the previously described Cu filter. Figure 8 shows the dose calculations with the whole Teflon spectrum and the two filters used during the experiment. The dose to the nucleus, that to the wall-membrane complex and that to the cytoplasm are reported. As expected the ratios between the dose to the nucleus and those to the other cell compartments are smaller with the Cu filter.

In order to take into account the variation of absorbed dose due to biological variability (different cells sizes) we considered the cell radii distribution obtained in a related work on the characterisation of yeast cells [8] (average radius = 2.58 μm; distribution width = 0.54 μm) and we calculated the doses delivered to cells of different size (the other typical cell parameters, *i.e.* wall-membrane thickness and nuclear radius, being scaled accordingly). Of course the dose to the nucleus decreases with increasing the cell radius (see Fig 9).

7 Source calibration

In order to calibrate the automatic dose control system used during the radiobiology experiment, it was necessary to relate the P-I-N output (in nC) to the dose delivered to the cells (in rad). Both these parameters depend on the absorbed energy integrated over the whole spectrum, so they are strongly connected with the spectral shape of emitted radiation. Since the filtering modifies the emitted spectrum, we needed two different calibrations (one for each sets of filters used in the experiment).

Considering the reconstructed spectrum, and normalising the radiation intensity of the whole spectrum at 1 mJ cm^{-2}, we obtain the values of 4.174×10^3 nC, with the Cu filter and 1.785×10^4 nC with the Al filter for the charge collected at the P-I-N diode.

The source incident radiation (1 mJ/cm^2) to the average cell with undifferentiated composition corresponds to a dose of 1.11×10^4 rad when the Cu filter is used and

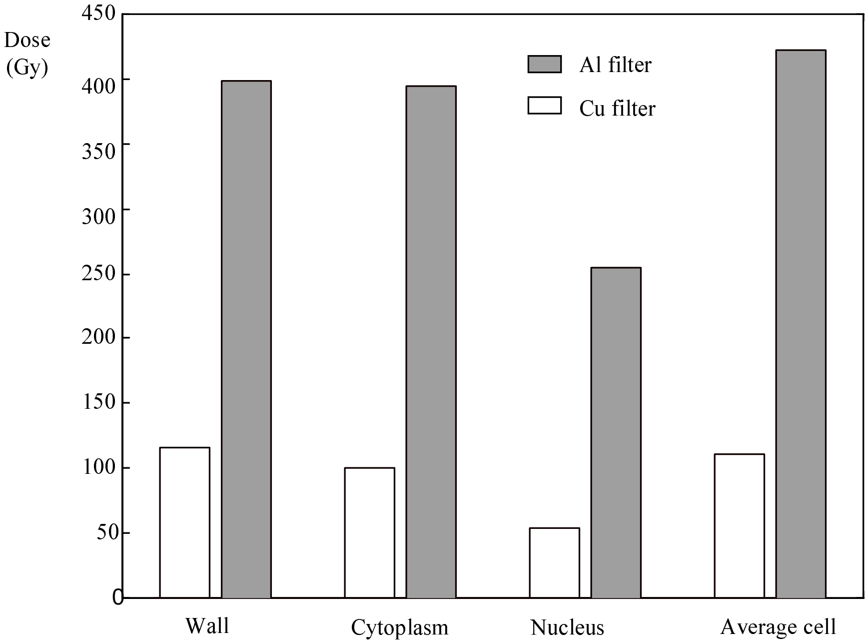

Fig. 8. Dose to mean cell delivered by Teflon radiation. Calculations are performed with the reconstructed spectrum normalised to 1 mJ cm^{-2} before filters.

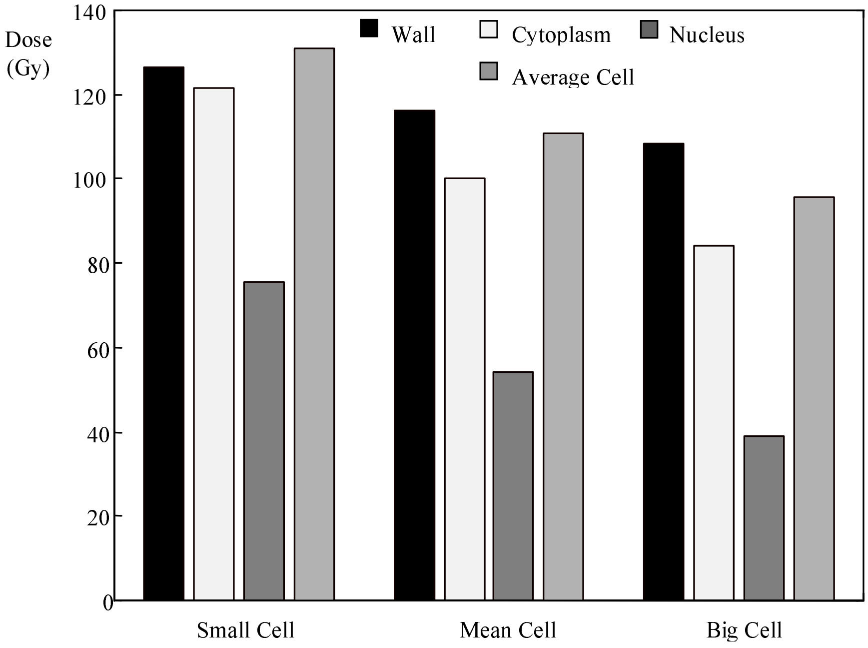

Fig. 9. Doses to different cell compartments as a function of cell dimension.

of 4.32×10^4 rad with the Al filter. Thus to deliver 1 rad of dose to the "average undifferentiated" cell, the irradiation has to be stopped when the summed value read by P-I-N reaches 0.376 nC with Cu filter or a value of 0.413 nC in the case of Al filter.

8 Conclusions

In conclusion, we obtained an accurate spectroscopic characterisation of a laser plasma X-ray source, that allowed a quite precise estimation of the dose deposited in the considered micro-organism. The cellular model presented in the paper granted the calculation of the dose in the three major cell compartments, taking into account the biological variability (*i.e.* cell dimensions) and the realistic features of the X-ray spectrum. These results have consequences at biological level, since they allow to characterise dose deposition in the cell and give some hints on which biological damages are more likely to occur and where. We recall again that on the contrary, the usual approach in microbiology is based on the evaluation of surface dose and penetration depth in undifferentiated biological material.

Other important results were the source calibration with the P-I-N diode, allowing an automatic control of the delivered dose, and the choice of a set of filters which minimises the interaction with the nucleus, *i.e.* the genetic material, enhancing that with the external structures (wall and cytoplasm).

Concerning the plasma physics side of the experiment, we could characterise the produced plasma emission, highlighting that the spectrum was composed by two different contributions: one from a hot region ($T_\mathrm{e} \approx 130$ eV), with an important fluorine K shell emission, and the other of a colder region ($T_\mathrm{e} \approx 74$ eV), with mainly carbon K shell emission. These results are in a very good agreement with the numerical simulations from the code RATION.

The emission, the temperature ($T_\mathrm{h} \approx 14$ keV) and the number ($n_\mathrm{h} \approx 0.15 n_\mathrm{e}$) of the suprathermal electrons could be evaluated and the results are comparable with those already present in literature. The total laser energy to hard X-rays conversion efficiency η can be estimated by integrating equation (6) over all photon energies and multiplying for the plasma volume V which we assume to be half a sphere of diameter ≈ 35 μm. In this way we get $E_x \approx 0.02$ mJ or $\eta \approx 10^{-4}$ if we consider that $E_\mathrm{L} \approx 300$ mJ.

The energy absorbed in suprathermal electrons is $E_\mathrm{h} \approx n_\mathrm{h} V T_\mathrm{h} \approx 16$ mJ or 5% of laser energy. Although the evaluation of E_x and E_h is influenced by the value of V, which is not precisely known, still the E_h value is remarkable considering that we have used a laser which is quite small and also operating in ultra-violet (which minimised hot electron generation [28]). Values of $\approx 30\%$ have been obtained [29] at intensities of the order of a few 10^{16} W/cm^2 by using a much bigger laser system operating in the infrared. However this result may be explained by considering how some recent theoretical and numerical works [30] have shown that the presence of a long plasma, eventually produced by a laser pre-pulse, drastically affects hot electron generation. In our case such an effect is of course enhanced because we are dealing with a train of picosecond laser pulses.

The experiment has been realised at Rutherford Appleton Laboratory in the framework of the EU "Access to Large Scale Facilities" Programme. We also acknowledge the contribution of the Italian MURST under the research program "Interaction of plasmas with nanosecond and picosecond lasers".

Appendix A: Film deconvolution model

A.1 Crystal reflectivity

Considering the X-ray energy range of interest (λ between 10 and 17 Å) we used a RbAP crystal with spacing $2d = 26.121$ Å. Data on integrated crystal reflectivity were obtained from [31]. They show that in the case of a RbAP crystal it is possible to ignore the reflectivity at higher orders since these are less then one tenth of the first order reflectivity.

In order to use these data to evaluate the crystal peak reflectivity, *i.e.* the reflection coefficient, *vs.* photon energy, we needed to know the corresponding rocking angle $\Delta\vartheta$ that has been calculated with the formula:

$$\Delta\vartheta = 0.112 N|F| d (1 + \cos 2\vartheta_\mathrm{B}) / \sin\vartheta_\mathrm{B} \qquad \text{(A.1)}$$

given in [32] where ϑ_B is the Bragg angle and $\Delta\vartheta$ is expressed in eV. From the theoretical curve reported by the same authors we deduced a value $N|F| = 0.205$ Å^{-3} for the RbAP crystal. The crystal reflection coefficient is then given by the ratio of the integral reflectivity to the rocking angle.

A.2 Film sensitivity

As for film response we used the model proposed by Henke [33, 34] according to which the optical density is given by:

$$\alpha D_{0.1} = a \ln(1 + b\beta I) \qquad \text{(A.2)}$$

where I (No. photons μm^{-2}) is the radiation intensity, $D_{0.1}$ is the net optical density at 0.1 numerical aperture, $a = 0.68$ μm^{-1} and $b = 1.69$ μm^2 are the values obtained by Henke interpolating different sets of experimental data, finally α and β are wavelength dependent parameters which are given by [33, 34] as $\alpha = (d_0 + \sin\theta/\mu')^{-1}$ and $\beta = [1 - \exp(-\mu_1 d)]\exp(-\mu_0 t_0 / \sin\theta)$.

Here μ_0, μ_1, μ', expressed in cm^{-1}, are respectively the linear absorption coefficients of film gelatine ($C_8H_{15}O_5N_2$ with a density $\rho_0 = 1.4$ g cm^{-3}), of AgBr, present in the film ($\rho_1 = 6.473$ g cm^{-3}) and of the etherogeneous emulsion. The last coefficient is found in [33, 34] as $\mu' = \mu_0 - \ln\{1 - V[1 - \exp(-(\mu_1 - \mu_0)d)]\}/d$, where $V = 0.4$ [33] is the volume fraction occupied by AgBr grains in the emulsion, $d = 1.3$ μm [35] is the dimension of AgBr grains, $t_0 = 1$ μm [33] is the thickness of the supercoat gelatine and θ is the radiation incidence angle on the film that depends on the Bragg angle and on the spectrometer geometry.

We used the Kodak DEF film at energies lower than those considered by Henke in his work [33]. Hence we needed to change the parameters of Henke's model to adapt it to our experimental conditions. The use of very low energy photons implies that only the first layer of the emulsion is really active. Thus we considered a non zero value for d_0, the thickness of the first emulsion layer that mainly absorbs the X-rays below 1 keV. From data reported in [34] relative to different kind of films, we estimated a value $d_0 = 0.55$ μm for Kodak DEF.

Finally, since our microdensitometer gave the film net diffuse optical density D_d, we used the relation [33]:

$$D_{0.1}/D_\mathrm{d} = 1.98 - 0.35 D_\mathrm{d} + 0.09 D_\mathrm{d}^2 \qquad \text{(A.3)}$$

to convert diffuse density to the specular density used in Henke's work.

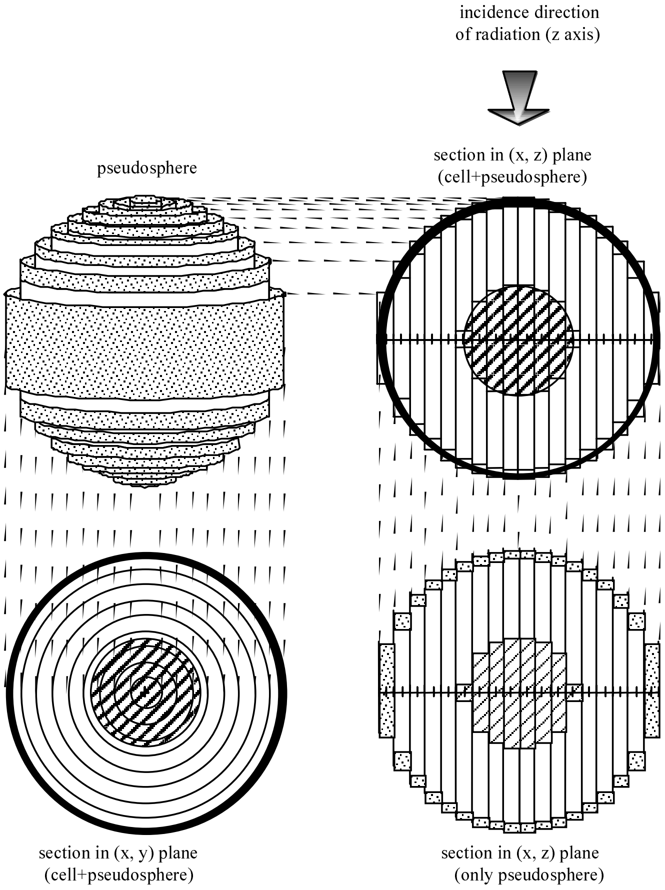

Fig. 10. Cellular model.

Appendix B: Cellular model and dose calculation

The cellular model used is showed in Figure 10: the program approximates the cell with a pseudo-sphere constituted by cylindrical coaxial layers, their axis being the X-ray incidence direction (z-axis). The mean radius of the ith cylindrical layer is r_i and, depending on whether $r_i < R_{\text{nucleus}}$, $R_{\text{nucleus}} < r_i < R_{\text{cytoplasm}}$ or $R_{\text{cytoplasm}} < r_i < R_{\text{cell}}$, such a layer is divided in z-direction in 5, 3 or 1 different compartments. Hence it is possible to calculate the radiation attenuation through each compartment of the specific cylindrical layer and the energy deposition. The total energy deposition in each single cell compartment is thus given by the sum of the energies deposited in the corresponding elements of all cylindrical layers. The dose is simply given by the ratio between this energy and the compartment mass (here the exact volume of the spherical layer is calculated instead of the approximated one which would introduce a further error). Obviously the approximation degree depends on the number n of the cylindrical layers considered and the accuracy increases with n. Note that the deposited energy sums u while the doses do not sum!

In order to give an evaluation of the approximation introduced with our model, we made a comparison between the dose calculation in the case of the "average" undifferentiated cell, which can be obtained analytically, and the values obtained with our program. The analytical calculation follows the same principle used by the program and consider an infinitesimal thickness (dx) of the cylindrical layer. The energy absorbed by the infinitesimal volume of the sphere with a radius between x and $x + \mathrm{d}x$ is $\mathrm{d}E(x) = (I(x), \underline{n})\mathrm{d}A$. Here $\underline{n}$ is the unit vector normal to the spherical surface at the point of radiation incidence, and dA is the area in the normal plane. Radiation falling onto the spherical surface in a point at a distance x from the centre, on the plane perpendicular to the incidence direction, makes a path inside the cell with length $z = 2(R^2 - x^2)^{1/2}$, undergoing an attenuation $\exp(-\mu z)$.

Hence $\mathrm{d}E(x) = 2\pi I_0[1-\exp(-\mu z(x)]x\mathrm{d}x$ and the total energy deposed in the whole sphere is

$$\begin{aligned} E &= \int_0^R \mathrm{d}E = 2\pi I_0 \int_0^R \left\{1 - \exp[-2\mu(R^2 - x^2)^{1/2}]\right\} x\mathrm{d}x \\ &= 2\pi I_0 \left[\frac{R^2}{2} - \frac{1-(1+2\mu R)\exp(-2\mu R)}{\mu^2}\right] \qquad \text{(B.1)} \end{aligned}$$

The dose is simply given (in Gy) by making the ratio between this value (in mJ) and the cell mass (in g), and we recall that 1 Gy = 100 rad.

References

1. E. Turcu, I.N. Ross, P. Trenda, C.W. Wharton, R.A. Meldrum, H. Daido, M.S. Schulz, P. Fluck, A.G. Michette, A.P. Juna, J.R. Maldonado, H. Shields, G.J. Tallents, L. Dwivedi, J. Krishnan, D.L. Stevens, T.J. Tenner, D. Batani, H. Goodson, Picosecond Excimer Laser-Plasma X-ray Source for microscopy, biochemistry and lithography, in *Applications of Laser Plasma Radiation*, Proc. SPIE **2015**, 243 (1994).
2. M. Milani, A. Conte, M. Costato, F. Salsi, G. Baroni, D. Batani, L. Ferraro, E. Turcu, Eur. Phys. J. D **5**, 267 (1999).
3. D. Batani, A. Masini, M. Milani, M. Costato, A. Pozzi, E. Turcu, N. Lisi, F. Musumeci, A. Triglia, Nuovo Cimento D **18**, 657 (1996).
4. A. Masini *et al.*, X-ray irradiation of yeast cells, in Applications of X-rays generated from lasers and other bright sources, San Diego, Proc. SPIE **3157**, 203 (1997).
5. A. Masini, D. Batani, F. Previdi, M. Costato, A. Pozzi, E. Turcu, R. Allott, N. Lisi, Eur. Phys. J. AP **5**, 267 (1998).
6. M.F. Tuite, S.G. Oliver, *Saccharomyces* (Plenum Press, New York, 1991).
7. F.M. Klis, Yeast **10**, 851 (1994).
8. D. Batani, A. Masini, E. Conte, C. Lora Lamia Donin, F. Cotelli, M. Moret, A. Pozzi, M. Costato, E. Turcu, N. Lisi, R. Allot, Phys. Medica **14**, 4 (1998).
9. F.N. Beg, A.R. Bell, A.E. Dangor, C.N. Danson, A.P. Fews, M.E. Glinsky, B.A. Hammel, P. Lee, P.A. Norreys, M. Tatarakis, Phys. Plasmas **4**, 2 (1997).
10. C.E. Max, in *Laser Plasma Interaction*, edited by R. Balian, J.C. Adams (North Holland Publishing Company, Amsterdam, 1982).
11. J.A. Bearden, A.F. Burr, Rev. Mod. Phys. **39**, 125 (1967).
12. F. Bijkerk, E. Louis, M. van der Wiel, E. Turcu, G.J. Tallents, D. Batani, J. X-ray Sci. Tech. **3**, 133 (1992).

13. M. Vollbrecht, RATP, `mvollbr@roetgen.physik.uni-jena.de`, 1995.
14. B. Henke, in *X-ray data booklet*, Center for X-ray optics (Lawrence Berkley laboratory, University of California, 1986).
15. R.L. Kelly, Phys. Rev. A **34**, 6 (1986).
16. I. Hutchinson, *Principles of plasma diagnostics* (Cambridge University Press, Cambridge, 1987).
17. G.J. Tallents, *X-Ray Spectroscopy of Tokamaks* JET, Joint European Torus, Reports N.JET-P(87)56.
18. D. Colombant, G. Tonon, J. Appl. Phys. **44**, 8 (1973).
19. R.W. Lee, *User Manual for RATION* (Lawrence Livermore National Laboratory, 1990).
20. R.L. Kelly, NRL Report (1968).
21. C.E. Max, Physics of the coronal plasma in laser fusion targets, in *Laser-Plasma Interactions*, edited by R. Balian, J.C. Adam (North Holland Pub., Amsterdam, 1982)
22. D.W. Forslund, J.M. Kindel, K. Lee, Phys. Rev. Lett. **39**, 284 (1977); J.D. Hares *et al.*, Phys. Rev. Lett. **42**, 1216 (1979); M.D. Rosen *et al.*, Phys. Fluids **22**, 2020 (1979); R.J. Harrach, R.E. Kidder, Phys. Rev. A **23**, 887 (1981).
23. D.J. Bond, J.D. Hares, J.D. Kilkenny, Plasma Phys. **24**, 91 (1982); B. Luther Davies, A. Perry, K.A. Nugent, Phys. Rev. A **35**, 4306 (1987).
24. Goodfellow Catalogue, `www.goodfellow.com`.
25. G.S. Landsberg, *Optica* (Nauka, Moscow, 1979).
26. D. Frankenberg *et al.*, Int. J. Radiat. Biol. **50**, 727 (1986).
27. M. Costato *et al.*, Phys. Medica **13**, 263 (1997).
28. M.H. Key, Energy transport in laser-produced plasmas, in *Physics of laser plasmas*, edited by A. Rubenchik, S. Witkowski (North Holland Pub., Amsterdam, 1991).
29. D. Batani, J. Davies, A. Bernardinello, T.A. Hall, M. Koenig, F. Pisani, A. Djaoui, N. Norreys, D. Neely, S. Rose, Phys. Rev. E **61**, 5725 (2000).
30. A. Pukov, J. Meyer-ter-Ven, in *Superstrong Fields in Plasmas*, edited by M. Lontano, G. Mourou, F. Pegoraro, E. Sindoni, Varenna, Proc. AIP **426**, 372 (1998).
31. B.L. Henke, P.A. Jaanimagi, Rev. Sci. Instrum. **56**, 8 (1985).
32. N.G. Alexandropoulos, G.G. Cohen, Appl. Spec. **28**, 2 (1974).
33. B.L. Henke, J.Y. Uejio, G.F. Stone, C.H. Dittmore, F.G. Fujiwara, J. Opt. Soc. Am. B **3**, 11 (1986).
34. B.L. Henke, S.L. Kwok, J.Y. Uejio, H.T. Takmada, G.C. Young, J. Opt. Soc. Am. B **1**, 6 (1984).
35. P.D. Rockett, C.R. Bird, C.J. Hailey, D. Sullivan, D.B. Brown, P.G. Burkhalter, Appl. Opt. **24**, 16 (1985).